Engineered interfaces for heterostructured intermetallic nanomaterials

Jiaqi Yu[1], Yadong Yin[2], Wenyu Huang[1,3]*

[1]Department of Chemistry, Iowa State University, Ames, Iowa 50010, United States

[2]Department of Chemistry, University of California, Riverside, California 92521, United States

[3]Ames National Laboratory, Ames, Iowa 50010, United States

*Corresponding author. Email: whuang@iastate.edu

Abstract:

Heterostructured nanomaterials are of interest for many applications due to their unique properties, which depend on the identity of each individual component and the interface between them. However, the difficulty in controlling the synthesis of heterostructures and the interfaces between components limits their applications. Here, we develop a colloidal synthetic method to prepare heterostructure intermetallic nanomaterials (iNMs) and engineer the interfaces between the individual components, based on the galvanic replacement mechanism and precisely controlled addition of precursors. Up to four distinct intermetallic phase-segregated segments could be combined in one nanoparticle. Nanometer-precision phase-segregated control along one dimension of iNMs was demonstrated by taking advantage of the layered growth pathway at the intermetallic-metal interfaces, leading to a maximum number of interfaces between different intermetallic phases. By adjusting the number of interfaces in a particle, we demonstrated a systematic control of the interface-to-bulk ratio in heterostructured iNMs. This method offers great potential for preparing complex heterostructured nanomaterials with controlled interfaces, enabling the exploration of their properties and applications.

Introduction

Nanomaterials with heterogeneous structures and multiple components are essential for designing next-generation materials in cross-field applications. The structure of each component and the interface between them determine the properties of heterostructured nanomaterials[1]. Much effort has been devoted to studying controllable synthesis with a large yield to fulfill the broad application of heterostructured nanomaterials. Nevertheless, only limited heterostructured nanomaterials have been produced, such as heterostructure metal sulfate[2] and metal alloys[3]. Interfaces, the boundary of each segment in heterostructures, generate structural discontinuity, alter the electronic structure and therefore, impact the properties and therefore the application of materials in different areas[4], including catalysis[5], dielectric devices[6], solar cells[7], mechanically superior materials[8], and quantum technology[9]. The capability to precisely control the interface cannot be overstated in understanding the fundamental properties of heterostructured nanomaterials for various applications. However, restricted by the limited nanoscale manipulation methodologies, achieving sub-nanometer and unit-cell-level controllable synthesis of heterostructured nanomaterials has remained challenging. Designing and preparing interface nanomaterials with maximized interface and tunable interface-to-bulk ratio in heterostructured nanomaterials is rarely achieved.

Intermetallic nanomaterials (iNMs), a subcategory of alloys with a defined stoichiometry and atomically ordered crystal structure, comprise an important family of materials with various applications, including catalysis[10-15] and biomedical theropy[16]. Although the formation of the ordered intermetallic crystal structure is thermodynamically favored, realizing the disorder-to-order transformation requires the overcoming of energy barriers. Traditional intermetallic synthesis methods usually involve high-temperature treatments, which makes the morphology and structure of iNMs poorly controllable[17]. Some methods were developed to preserve the morphology and control the particle size of iNMs, such as support modification[17,18], templated synthesis[19,20], and chemical vapor deposition[21]. Colloidal synthesis, including hydrothermal and polyol processes, can avoid high-temperature treatments by forming iNMs directly from metal ions[22,23]. Nonetheless, synthesizing desired heterostructured iNMs is extremely challenging, commonly resulting in the thermodynamically favored homostructured iNMs[24]. The successful demonstration of heterostructured iNMs is rare and limited to only certain metals with simple structures[25], while the demonstration of interface materials and adjusting interface-to-bulk ratio in iNMs face incredible difficulties.

Herein, we constructed an intermetallic nanomaterials library containing heterostructured and interface iNMs using simple benchtop chemistry. Heterostructured iNMs with both single and multiple intermetallic phases were demonstrated, and up to 4 distinct intermetallic segments segregated in one single nanoparticle were successfully prepared. The synthetic process is governed by the galvanic replacement mechanism[26,27], during which metal ions with more positive electrochemical reduction potentials are reduced by metals with more negative reduction potentials and plated in the active metal templates. Although galvanic replacement has been well-developed in nanomaterials synthesis, such as metal[28-31] and metal oxide nanomaterials[32,33], the capability of galvanic replacement in synthesizing intermetallic nanomaterials has not yet been demonstrated. The controllability of galvanic replacement that enables nanometer-precision manipulation and systematic study makes it an attractive method for heterostructured iNMs synthesis. Minimizing the interfacial energy during the galvanic replacement leads to interface growth of heterostructures. For iNMs with minor lattice mismatches, secondary iNMs selectively grow from the interface.

This interface growth mechanism facilitates unit-cell-level interface engineering in heterostructures, where multiple phase-segregated segments of unit-cell thickness are synthesized in one single particle. We term such materials as interface iNMs, in which no bulk intermetallic phase exists. In addition, changing the number, and thus the thickness, of phase-segregated segments enables the tunable interface-to-bulk ratio in heterostructured iNMs.

Synthetic strategy demonstration using single component iNMs

We chose Sn as the primary templating metal NPs to demonstrate the development of the galvanic replacement method. In a three-neck flask connected to a Schlenk line, Sn nanoparticles (NPs) were synthesized by hot injection of appropriate precursors into a heated oleylamine media (shown in Extended Data Fig. 1a and Supplementary Fig. 1). Metal ion precursors (M^{n+}) were then injected into the same colloidal solution containing the Sn NPs, and the addition rate was controlled using a syringe pump (synthesis setup shown in Supplementary Fig. 2). With the addition of M^{n+}, galvanic replacement happened, where electrons transferred from Sn NPs to M^{n+} driven by the electrochemical potential differences. Since Sn NPs are air-sensitive, the whole synthesis process was operated under Ar protection. During the addition of a single M^{n+}, Janus intermetallic M_xSn_y-Sn NPs were initially formed (for example Ni_3Sn_4-Sn iNMs in Supplementary Fig. 3 and $PdSn_4$-Sn iNMs in Supplementary Fig. 4), followed by further conversion to pure-phase M_xSn_y iNMs. Once the M_xSn_y intermetallic compound was formed, adding excess M^{n+} would not change the intermetallic structure because the atomically ordered structure stabilizes the Sn atoms and prevents them from participating in further galvanic replacement reactions.

A series of single component metal-tin iNMs were prepared through the galvanic replacement method (Extended Data Fig. 1), which served as the foundation for synthesizing heterostructured iNMs. Several metals, such as Pt, Pd, and Rh, form an MSn_4 (M = Pt, Pd, and Rh) intermetallic phase with the same Ccce crystal structure (Extended Data Figs. 1b-d and Supplementary Figs. 5-10). MSn_4 intermetallic compounds have a special "Sn-M-Sn" layered structure with weak interactions between layers. MSn_4 single crystals are topological semimetals with interesting physical properties, including ultrahigh magnetoresistivity, high carrier mobility, and low resistivity[34]. Due to the layered crystal structure, the as-synthesized MSn_4 iNMs have a platelet morphology, differing from the original spherical Sn NPs. Some other M_xSn_y iNMs, for example Cu_6Sn_5, and Ni_3Sn_4, were also prepared, resulting in spherical iNMs (Extended Data Figs. 1f-I and Supplementary Figs. 11-20). Ccce structured $AuSn_4$ iNMs are much less stable than $P6_3/mmc$ AuSn intermetallic structure according to the phase diagram and formation energy, so only with special treatments (quenched with dry ice/isopropanol bath, details in the Method section) can $AuSn_4$ intermetallic structure be preserved as a few layers on the edge of NPs (Extended Data Fig. 1e and Supplementary Figs. 21-23).

Heterostructured intermetallic nanomaterials

The above examples demonstrate the structural versatility achieved in iNMs through the galvanic replacement synthetic strategy, based on which we envisaged that heterostructured phase-segregated iNMs with different structures and elemental constituents could be realized by precisely control the amount and the addition order of different M^{n+} precursors into Sn NPs solutions. Galvanic replacement reactions between M^{n+} and Sn NPs and the formation of intermetallic phases

occur according to the sequence of M^{n+} additions (Supplementary Figs. 24-27). As an illustration, $PtSn_4$-Cu_6Sn_5 iNMs shown in Fig. 1a were synthesized between distinct intermetallic phases presenting Janus morphology with $PtSn_4$ plates on one side of Cu_6Sn_5 spheres. The separation of Pt-Sn and Cu-Sn domains and atomic ratio (Pt/Sn = 0.25, Cu/Sn = 1.2) from the energy dispersive X-ray spectroscopy (EDS) line profile further proved the formation of phase-segregated heterostructured $PtSn_4$-Cu_6Sn_5 iNMs (Supplementary Fig. 25). When Pt, Pd, and Cu precursors were added in order, iNMs containing three intermetallic segments were obtained, with $PdSn_4$ between $PtSn_4$ and Cu_6Sn_5 forming a "burger" structure (Fig. 1b and Supplementary Fig. 28-29). In this heterostructured iNM, there are two interfaces, $PtSn_4$-$PdSn_4$ and $PdSn_4$-Cu_6Sn_5. As mentioned above, $PtSn_4$ and $PdSn_4$ share the same "Sn-M-Sn" layered crystal structure. The interface between $PtSn_4$ and $PdSn_4$ consists of two Sn layers connected with weak Sn-Sn interaction and a minor lattice mismatch. Adding a fourth metal ion (Pt^{2+}, Pd^{2+}, Au^{3+}, and Cu^{2+}) to the system results in nanomaterials with four intermetallic segments, $PtSn_4$-$PdSn_4$-AuSn-Cu_6Sn_5 (Fig. 1c and Supplementary Figs. 30-33) and generates several different interfaces between intermetallic phases having same crystal structures ($PtSn_4$-$PdSn_4$), different crystal structures but small lattice mismatch ($PdSn_4$-AuSn), different crystal structure and large lattice mismatch (AuSn-Cu_6Sn_5). The synthesized heterogeneous iNMs with several phase-segregated segments provide a potential iNMs library for application across fields such as catalysts, where the interfaces in the heterostructured iNMs could be the active sites for catalytic reactions. Although it is possible to synthesize iNMs with more segments, we stopped at four intermetallic compounds due to the increased challenge of characterizing these iNMs (Supplementary Figs. 34-39).

To explore the possibility of preparing heterostructured iNMs with the same elemental constituents but different intermetallic phases, purely adding more M^{n+} does not convert the formed intermetallic phase to another phase. However, changing the precursor addition rate as a kinetic parameter could lead to different intermetallic phases, for example, $PdSn_3$-$PdSn_4$ iNMs (Fig. 1d and Supplementary Fig. 40). Like $PdSn_4$, $PdSn_3$ also has a layered crystal structure, but each layer is composed of "Sn-Pd-Sn-Pd-Sn" rather than "Sn-Pd-Sn" in $PdSn_4$. High-resolution scanning transmission electron microscopy (HR-STEM) imaging from the [100] direction of the synthesized iNMs reveals the separation of "Sn-Pd-Sn-Pd-Sn" layers along the $PdSn_3$ [010] direction from the "Sn-Pd-Sn" layers along the $PdSn_4$ [010] direction in a single particle, indicating the successful preparation of phase segregated hybrid $PdSn_3$-$PdSn_4$ nanoplates (Figs. 1d-e). Inspection of the intermediate of $PdSn_3$-$PdSn_4$ nanoplates (Fig. 1f) suggests that because of the minimized energy and fast atom diffusion at interfaces, the $PdSn_3$-$PdSn_4$ intermetallic grows from one side to the other side of the particle in a layer-by-layer fashion. The orientation of the Sn atom columns changed at the interface of Sn-$PdSn_4$.

Heterostructured iNMs growth mechanism study

The general applicability of the developed synthetic system to iNMs synthesis allowed a systematical study on nucleation and growth of heterostructured intermetallic materials. Intermediates showing the growth of intermetallic structures with the same and different space groups were obtained. Starting from intermetallic-Sn nanomaterials, we proposed two ways to grow the secondary intermetallic phases, including interfacial growth between the first intermetallic and Sn or direct nucleation from the other parts of the Sn template. $PtSn_4$ and $PdSn_4$ share the same space group and have a small lattice mismatch (< 1%). Therefore, to avoid

generating a new interface with Sn and minimize the interface distortion, the growth of $PdSn_4$ initiates at the interfaces of $PtSn_4$ and Sn (Fig. 2a and Supplementary Fig. 41-42). Similarly, the AuSn intermetallic phase follows the interfacial growth, starting from the interface of $PdSn_4$ and Sn (Fig. 2b and Supplementary Fig. 43-44), even though the crystal structure of AuSn ($P6_3/mmc$) is different from MSn_4 (Ccce) (M = Pt, Pd, and Rh). The growth pattern of AuSn to $PdSn_4$ and Sn suggests that the interface growth is applicable to intermetallic phases with different space groups. However, Cu_6Sn_5 with C2/c structure has a large lattice mismatch with Ccce MSn_4, so nucleation takes place randomly on the Sn segment (Fig. 2c and Supplementary Fig. 45-46).

The heterostructured iNMs growth mechanism observed from the intermediates is shown in the scheme in Fig. 2d. Using $PtSn_4$ and $PdSn_4$ as an example, for a small lattice mismatch between the new and existing intermetallic phases, the new intermetallic phase grows at the interface between Sn and the existing intermetallic phase. Combined with the observation of half MSn_4 layers intermediates (Fig. 1f), the new intermetallic phase growth between similar lattice structures could follow a layer-by-layer fashion from one side to the other. On the contrary, a large lattice mismatch leads to random nucleation on the Sn surface, such as the growth of Cu_6Sn_5 to MSn_4-Sn (Fig. 2c). Although the explanation of secondary intermetallic component growth mechanism focuses on the thermodynamics aspect—the lattice mismatch, kinetic factors could also contribute to the heterostructure growth mechanism.

Structural complex iNMs

The scope of the developed galvanic replacement-based preparation system could extend beyond heterostructured nanomaterials with several distinct segments. The layered growth mechanism studied above enables the precise control of the interface-to-bulk ratio in a single particle by adjusting the galvanic replacement conditions. The $PtSn_4$-$PdSn_4$ iNMs contain 2-7 or more alternating phase-segregated layers are shown in Fig. 3 and Supplementary Figs. 47-64. It is worth noting that each layer in a 7-segment iNM consists of a single unit-cell of MSn_4 along the [010] direction at this thickness, so only the "interface" exists in these iNMs — interface iNMs. It is generally accepted that the electronic structure and related properties of interfaces differ from bulk[35]; therefore, the ability to prepare interface nanomaterials and control the interface-to-bulk ratio could play a significant role in fundamental and mechanism studies across fields. From EDS mapping in Figs 3a-f, and Supplementary Figs. 47-60, successive additions of Pt and Pd precursor solutions in orders generated MSn_4 nanoplates with two, three, four, five, six, and seven layers of $PdSn_4$ and $PtSn_4$ display alternative layers along [010] direction, equivalent to achieving the adjustment of interface-to-bulk ratio. The alternating Pt and Pd peaks from the EDS line profile further confirmed the successful demonstration of heterostructured MSn_4 iNMs with several layers (Supplementary Figs. 48, 50, 54, 56, 58, and 60). While $PtSn_4$-$PdSn_4$ nanomaterials with multiple layers (9-10 layers), were achieved, which are also interface iNMs controlled at the sub-unit cell level, the characterization is challenging due to the limited spatial resolution of EDS mapping (Figs 3g and Supplementary Figs. 61-62).

The layered growth mechanism facilitates the extension of interfacial control from $PtSn_4$ and $PdSn_4$ to other intermetallic structures. Different from the $PtSn_4$-$PdSn_4$ iNMs which have one set of diffraction pattern, the diffraction pattern of $PtSn_4$-AuSn can be assigned to $PtSn_4$ and AuSn separately, representing a larger lattice mismatch (crystal structure analysis shown in Extended Data Fig. 2). Owing to the interface growth mechanism discussed above, interface iNMs between

$PtSn_4$, $PdSn_4$, and AuSn is plausible. As shown in Fig 4a, and Supplementary Figs. 65-73, heterostructured iNMs include $PtSn_4$-AuSn and $PtSn_4$-$PdSn_4$-AuSn intermetallic structures, with the intermetallic segment order matching the metal precursor adding sequence. A more complex structure was demonstrated between $PtSn_4$, $PdSn_4$, and AuSn, shown in Fig. 4b and Supplementary Fig. 74-75, where the three intermetallic structures repeat twice with the order of $PtSn_4$-$PdSn_4$-AuSn. Only interfaces exist in these $PtSn_4$-$PdSn_4$-AuSn iNMs, while the variety of interfaces is wider compared to binary $PtSn_4$-$PdSn_4$ iNMs, extending from interfaces between the same crystal structures to different crystal structures such as $PdSn_4$-AuSn and AuSn-$PtSn_4$. In addition, interface iNMs with up to 6-layer segregated intermetallic phases were obtained in $PtSn_4$-$PdSn_4$-$RhSn_4$ nanomaterials (Supplementary Figs. 76-81).

Other metal iNMs with structural complexity could also be rationally designed using this synthetic method. To study the generalizability, In NPs were used instead of Sn NPs as templates (Supplementary Fig. 82). Heterostructured Pt_3In_7-Rh_xIn_y iNMs were prepared by adding Rh and Pt precursors (Supplementary Figs. 83-87). The phase segregation can be clearly observed between Pt_3In_7 and Rh_xIn_y.

Conclusion

Heterostructured iNMs with phase segregation and structural complexity that would otherwise be unachievable have now been routinely designed and prepared. Up to four distinct phase-segregated intermetallic phases confined in a single nanoparticle were demonstrated, which enables interface study and growth mechanism insight between the same and different crystal space groups. Small lattice mismatch leads to the growth of new intermetallic components from the interface, while large lattice mismatch results in random nucleation. Based on the interface-induced growth mechanism, nanometer precision equivalent to unit-cell-level engineered synthesis is feasible, meaning iNMs with a maximized number of interfaces and tunable interface-to-bulk ratio can be prepared between the same and different intermetallic crystal structure groups. The successful preparation of interface nanomaterials makes the study of interface and mechanism perception feasible and will significantly impact multiple fields. In addition, the developed synthesis approach can be extended to prepare simple and structurally complex iNMs using benchtop chemistry and standard laboratory glassware.

Methods

Materials

Oleylamine (OAm, ≥98% primary amine, Aldrich), Tin (II) chloride anhydrous ($SnCl_2$, 98%, BTC), lithium bis(trimethylsilyl)amide ($LiN(SiMe_3)_2$, 97%, Aldrich), oleic acid (OA, 90%, Aldrich), tetrachloroethylene (TCE, ≥99%, Aldrich), diisobutylaluminium hydride (DIBAH, 1.0 M solution in tetrahydrofuran (THF), Aldrich), platinum (II) acetylacetonate ($Pt(acac)_2$, 98%, Acros Organics), palladium (II) acetate ($Pd(OAc)_2$, Oakwood Chemical), rhodium (III) acetylacetonate ($Rh(acac)_3$, 97%, Acros Organics), gold (I) chloride (AuCl, 97%, Strem Chemicals), gold (III) chloride trihydrate ($HAuCl_4$, ≥99.9% trace metals basis, Aldrich), copper (II) acetylacetonate ($Cu(acac)_2$, ≥99.0%, Merck), nickel (II) acetylacetonate ($Ni(acac)_2$, CHEM-IMPEX INT'L INC.), Tris(2,4-pentanedionato)ruthenium (III) ($Ru(acac)_3$, TCI), Tris(2,4-pentanedionato)cobalt (III) ($Co(acac)_3$, ≥98.0%, TCI), and Indium (III) chloride anhydrous ($InCl_3$, ≥99.0%, TCI) were used as received.

Synthesis Methods

All syntheses were carried out in an air-free Schlenk line system with a flow of ultra-high purity Ar (99.999%). The glassware was cleaned for at least 2 h in a base bath (saturated KOH in isopropanol/H_2O (1/1 v./v. ratio) solvent) and 10 min in freshly prepared aqua regia before rinsing with Milli-Q water (18.2 MΩ·cm at 25 °C) for 10 times and once with 200 proof ethanol (100%) and drying in an oven. The same cleaning procedure applies to stir bars. Septum, syringes, needles, and 6-dram vials were one-time use.

Synthesis of Sn NPs

Sn NPs were synthesized through a hot injection method[36]. In a 100 mL three-neck flask, 20 g of OAm was degassed at 140 °C under vacuum (<100 mTorr) for 1.5 h. After naturally cooling down to 50 °C, the flask was briefly opened, and 94 mg (0.5 mmol) of $SnCl_2$ powder was added under the flow of ultra-high purity argon. The mixture was heated up to 140 °C and degassed for another 30 min, followed by backfilling argon. With the addition of $SnCl_2$, the clear OAm solution changed to light yellow. In parallel, the $LiN(SiMe_3)_2$ toluene solution was prepared in a glovebox, where 1.204 g of $LiN(SiMe_3)_2$ was dissolved in 4 mL of dry toluene. At 210 °C, 2 mL of $LiN(SiMe_3)_2$/toluene solution was injected into the flask using a 5 mL syringe. After 10 s, 0.6 mL of DIBAH/THF (1 M DIBAH in THF) solution was injected rapidly using a 1 mL syringe. The color of the mixture turned dark brown immediately after adding the reducing reagent, DIBAH solution. After 6 h at 210 °C, the Sn NPs colloidal solution was cooled to room temperature using an ice water bath. During the cooling process, at around 100 °C, 10 mL of toluene was injected into the Sn NPs suspension. At room temperature, 20 mL of ethanol was added to precipitate the Sn NPs. The Sn NPs were separated through centrifuging for 4 min at 8000 rpm (8157 ×g). The precipitation was then redispersed in oleic acid/TCE solution (~ 6 mL, 2.4 mL OA in 120 mL TCE) for ligand exchange. Oleic acid has stronger coordination than OAm and can slow the oxidation process of Sn NPs in air. After ligand exchange, Sn NPs were precipitated by adding ethanol and centrifuging and redispersed in 6 mL of TCE solvent.

Synthesis of single composition M_xSn_y iNMs

M_xSn_y iNMs were synthesized through a one-pot, two-step method. Sn NPs synthesis was firstly set up following the procedure descript above. After 6 h at 210 °C, the mixture was cooled down to the galvanic replacement temperature, 120 °C, in 1 h. The secondary metal precursor solution

was prepared and degassed in the Schlenk line in a 50 °C oil bath. The metal precursor was then added to the Sn NPs colloidal solution controlled with a syringe pump using a 7-inch stainless steel needle. The tip of the needle touched the wall of the flask to enable continuous adding. The precursor solution preparation and adding rate are listed in Supplementary Table 1. After the galvanic replacement process, 1 h at 120 °C, the suspension was cooled down using a room temperature water bath. During the cooling, 10 mL of toluene was added. The suspension was divided into two centrifuge tubes containing 15 mL of ethanol each for centrifuging (4 min at 8157 ×g). The M_xSn_y iNMs were treated with ligand exchange and redispersed in 6 mL of TCE.

Special treatment to preserve $AuSn_4$ intermetallic structure

$AuSn_4$ intermetallic phase does not exist under room temperature. After the galvanic replacement, the mixture was quenched from 120 °C using a dry ice/isopropanol (IPA) bath. During the quenching process, 10 mL of toluene cooled in a dry ice/IPA bath was injected into the flask. After quenched to around 10 °C, the suspension was separated into two centrifuge tubes containing 15 mL of ethanol (cooled with dry ice/IPA bath) each for centrifuging (4 min at 8157 ×g) with centrifuge machine temperature set to 15 °C. The ligand exchange and washing were taken place with solvent or solution pre-cooled with a dry ice/IPA bath. The Au-Sn iNMs suspension was stored in the freezer, and the dry Au-Sn iNMs were stored at room temperature.

Synthesis of heterostructured iNMs

Heterostructured iNMs were synthesized with the same system. The metal precursor solution was prepared based on Supplementary Table 1 and was added successively. The adding sequence, amount of precursor, and the adding rate were summarized in Supplementary Tables 2-3. The interval between the two injections was 1 h, and the system was cooled down to room temperature 1 h after adding the last precursor. The post-reaction treatment procedure was the same as the single composition M_xSn_y iNMs.

Synthesis of single composition Rh_xIn_y NPs

Rh_xIn_y NPs were synthesized using the same method described in the "synthesis of single composition M_xSn_y iNMs" section. In NPs were firstly prepared in a 50 mL 3-neck flask under the Schlenk line following a reported method[37]. 0.125 mmol of $InCl_3$ (anhydrous) was added to 13 mL of OAm distilled for 1.5 h at 140 °C. The In-OAm solution was degassed under vacuum for another 45 min at 100 °C and followed with Ar flow. When the temperature was slowly raised to 150 °C, 2 mL of $LiN(SiMe_3)_2$/toluene (1.204 g $LiN(SiMe_3)_2$ dissolved in 4 mL toluene prepared in a glovebox) as ligand and 0.3 mL of DIBAH (1M in THF) as reductant were injected to the solution. After staying at 150 °C for 4 h, the In NPs were prepared. The suspension was cooled down to 120 °C in 20 min, and 1 mL of Rh precursor (0.042 mmol $Rh(acac)_3$ dissolved in 2 mL toluene) was added at a rate of 0.025 mL min^{-1}. After 1 h, the Rh_xIn_y NPs growth was stopped by quenching in a room-temperature water bath. 5 mL of toluene and 15 mL of ethanol were added, and the Rh_xIn_y NPs were precipitated by centrifuging at 8000 rpm (8157 ×g) for 4 min. The Rh_xIn_y NPs were treated with ligand exchange solution and redispersed in 3 mL of TCE.

Synthesis of heterostructured Pt_3In_7-In iNMs

In NPs were firstly prepared in a 50 mL 3-neck flask under a Schlenk line. When the In NPs colloidal solution was cooled down to 120 °C, 1.3 mL of Pt precursor (0.05 mmol $Pt(acac)_2$ dissolved in 1.3 mL OAm) was added at a rate of 0.025 mL min^{-1}. After 1 h, the heterostructured

Pt_3In_7-In iNMs growth was stopped by quenching in a water bath. 5 mL of toluene and 15 mL of ethanol were added, and the iNMs were separated by centrifuging at 8000 rpm (8157 ×g) for 4 min. The heterostructured Pt_3In_7-In iNMs were treated with ligand exchange solution and redispersed in 3 mL of TCE.

Synthesis of heterostructured Pt_3In_7-Rh_xIn_y iNMs

Similar to preparing Rh_xIn_y NPs, In NPs were firstly prepared in a 50 mL 3-neck flask under a Schlenk line. When the In NPs colloidal solution was cooled down to 120 °C, 0.35 mL of Pt precursor (0.016 mmol $Pt(acac)_2$ dissolved in 0.35 mL OAm) was added at a rate of 0.025 mL min^{-1}. After 1 h, 0.5 mL of Rh precursor (0.042 mmol $Rh(acac)_3$ dissolved in 2 mL toluene) was added at a rate of 0.025 mL min^{-1}. The heterostructured Pt_3In_7-Rh_xIn_y iNMs growth was stopped at 2 h by quenching in a water bath. 5 mL of toluene and 15 mL of ethanol were added, and the iNMs were precipitated by centrifuging at 8000 rpm (8157 ×g) for 4 min. The heterostructured Pt_3In_7-Rh_xIn_y iNMs were treated with ligand exchange solution and redispersed in 3 mL of TCE.

Characterizations

Transmission electron microscopy (TEM) images were obtained using a TECNAI G2 F20 operated at 200 kV. High-angle annular dark-field scanning transmission electron microscopy (HAADF-STEM) was performed on a Titan Themis 300 equipped with gun monochromator and probe spherical aberration (Cs) corrector operated at 200 kV. Gatan Digital Micrograph software was used for image processing. The energy dispersive X-ray spectroscopy (EDS) mapping data was collected with a Super-X EDX detector and was processed with ESPRIT 1.9 software. Powder X-ray diffraction (PXRD) was performed on a Bruker D_8 Advance Twin diffractometer using Cu $K_{\alpha 1}$ radiation (40 kV, 40 mA, λ = 0.1541 nm). A knife was placed ~ 2 mm above the samples during the measurement.

To prepare PXRD sample, 2 mL of as-synthesized iNMs was mixed with 10 mL of ethanol. The solvent was removed after centrifuge. After washing with ethanol once, the iNMs were redispersed in ~1 mL ethanol and dried at room temperature under vacuum. The dried iNMs became dark brown powder and were placed on a silicon wafer for the PXRD measurement.

To prepare TEM sample for high-resolution imaging and EDS mapping, 20 μL of iNMs in TCE was washed with hexanes and ethanol mixture solvent (1/1 V./V. ratio) 3 times to remove ligand on the iNMs. After washing, the iNMs were dispersed in 100 μL hexanes and drop-cast onto the TEM grids. Au TEM grid was used for the sample containing Cu element, and Ni TEM grid was used for the sample containing both Cu and Au elements. For all the other samples, regular Cu grids were used. Before obtaining STEM images, beam showering was performed to prevent coke deposition during the measurement. In the beam showing process, the sample was treated with 11 nA beam under conventional TEM mode for 10 min.

To prepare TEM sample for low-resolution imaging, 10 μL of iNMs TCE suspension was directly drop-cast onto the TEM grid and dried neutrally in air. The choice of the TEM grid is the same as the sample for high-resolution imaging. STEM images were obtained without beam treatment.

Data Availability: All data are available in the main text and the supplementary materials.

Supplementary Information

Supplementary Discussion

Supplementary Figs. 1-87

Supplementary Tables 1-3

Acknowledgments: JY and WH acknowledge the support from National Science Foundation grant CHE-2108307 and Iowa State University Trapp Award. JY thanks Dr. Robert Angelici for his valuable discussion and suggestion on the manuscript. Authors acknowledge Dr. Kirill Kovnir and Dr. Julia Zaikina for the valuable discussions and suggestions on XRD characterization.

Author contributions: JY, YY, and WH designed the conceptualization, methodology and visualization of this project. JY performed all the experiments and drafted the original manuscript under the supervision of WH. YY and WH revised and edited the manuscript.

Competing interests: Authors declare that they have no competing interests.

Figure Captions:

Fig. 1 | Heterostructured iNMs with varying elemental constituents. (a-c) High-angle annular dark-field scanning transmission electron microscopy (HAADF-STEM) image and energy dispersive X-ray spectroscopy (EDS) mapping of heterostructured iNMs $PtSn_4$-Cu_6Sn_5 (a), $PtSn_4$-$PdSn_4$-Cu_6Sn_5 (b), $PtSn_4$-$PdSn_4$-AuSn-Cu_6Sn_5 (c); (d) HAADF-STEM image of heterostructured $PdSn_3$-$PdSn_4$ iNMs; (e) crystallographic projection of $PdSn_3$ and $PdSn_4$ from [100] direction; (f) high resolution-STEM (HR-STEM) image of $PdSn_3$-$PdSn_4$ intermediate, with inserted colored image demonstrating 3 segments (green: Sn, red: $PdSn_4$, blue: $PdSn_3$).

Fig. 2 | Heterostructured iNM growth mechanism. (a-c) Energy dispersive X-ray spectroscopy (EDS) mapping images of intermediates illustrating the growth of $PdSn_4$ to $PtSn_4$-Sn (a), AuSn to $PtSn_4$-$PdSn_4$-Sn (b), and Cu_6Sn_5 to $PtSn_4$-$PdSn_4$-Sn (c). In the EDS mapping images, red represents Pt element, cyan represents Pd, yellow represents Au, blue represents Cu, and grey represents Sn. (d) Scheme illustrating the layered growth mechanism of heterostructured iNMs using $PtSn_4$ and $PdSn_4$ as examples.

Fig. 3 | Heterostructured iNMs with structural complexity through layered growth. High-angle annular dark-field scanning transmission electron microscopy (HAADF-STEM) images and energy dispersive X-ray spectroscopy (EDS) mapping of $PtSn_4$-$PdSn_4$ iNMs (a), 3 layers "sandwich" structure $PtSn_4$-$PdSn_4$-$PtSn_4$ iNMs (b), and 4 layers (c), 5 layers (d), 6 layers (e), 7 layers (f), and multiple layers (g) of $PtSn_4$-$PdSn_4$ iNMs. Due to the spatial resolution limits of EDS mapping, the elemental enrichment of each layer in (g) can hardly be separated. However, with the clear z-contrast between Pt and Pd elements from the HR-STEM, multiple bright and dark alternatives represent $PtSn_4$ and $PdSn_4$, respectively. The number of layers in (g) is approximately

9-10 layers counted by the number of dark and grey alternatives from STEM image, while the numbers of layers in (a-f) are counted based on the EDS mapping.

Fig. 4 | Heterostructured and interface iNMs with extended interface variety. High-angle annular dark-field scanning transmission electron microscopy (HAADF-STEM) images and energy dispersive X-ray spectroscopy (EDS) mapping of 3 layers (a) and 6 layers (b) of $PtSn_4$-$PdSn_4$-AuSn iNMs. 6 layer $PtSn_4$-$PdSn_4$-AuSn iNMs are interface iNMs, while 3 layer iNMs represent the tunable interface to bulk ratio. The type of interface includes $PtSn_4$-$PdSn_4$, $PdSn_4$-AuSn, and AuSn-$PtSn_4$.

References

1 Steimle, B. C., Fenton, J. L. & Schaak, R. E. Rational construction of a scalable heterostructured nanorod megalibrary. *Science* **367**, 418-424, doi:10.1126/science.aaz1172 (2020).

2 Fenton, J. L., Steimle, B. C. & Schaak, R. E. Tunable intraparticle frameworks for creating complex heterostructured nanoparticle libraries. *Science* **360**, 513-517, doi:doi:10.1126/science.aar5597 (2018).

3 Chen, P.-C. *et al.* Polyelemental nanoparticle libraries. *Science* **352**, 1565-1569, doi:doi:10.1126/science.aaf8402 (2016).

4 Sun, X. *et al.* Dislocation-induced stop-and-go kinetics of interfacial transformations. *Nature* **607**, 708-713, doi:10.1038/s41586-022-04880-1 (2022).

5 Du, K. *et al.* Interface engineering breaks both stability and activity limits of RuO2 for sustainable water oxidation. *Nat. Commun.* **13**, 5448, doi:10.1038/s41467-022-33150-x (2022).

6 Zhang, H. *et al.* Atomically engineered interfaces yield extraordinary electrostriction. *Nature* **609**, 695-700, doi:10.1038/s41586-022-05073-6 (2022).

7 Gong, Y. *et al.* Elemental de-mixing-induced epitaxial kesterite/CdS interface enabling 13%-efficiency kesterite solar cells. *Nat. Energy*, doi:10.1038/s41560-022-01132-4 (2022).

8 Chen, K. *et al.* Graphene oxide bulk material reinforced by heterophase platelets with multiscale interface crosslinking. *Nat. Mater*, doi:10.1038/s41563-022-01292-4 (2022).

9 Su, C. *et al.* Tuning colour centres at a twisted hexagonal boron nitride interface. *Nat. Mater* **21**, 896-902, doi:10.1038/s41563-022-01303-4 (2022).

10 Zhong, M. *et al.* Accelerated discovery of CO2 electrocatalysts using active machine learning. *Nature* **581**, 178-183, doi:10.1038/s41586-020-2242-8 (2020).

11 Huang, X. *et al.* High-performance transition metal-doped Pt3Ni octahedra for oxygen reduction reaction. *Science* **348**, 1230-1234, doi:doi:10.1126/science.aaa8765 (2015).

12 Zhou, M., Li, C. & Fang, J. Noble-Metal Based Random Alloy and Intermetallic Nanocrystals: Syntheses and Applications. *Chem Rev* **121**, 736-795, doi:10.1021/acs.chemrev.0c00436 (2021).

13 Furukawa, S. & Komatsu, T. Intermetallic Compounds: Promising Inorganic Materials for Well-Structured and Electronically Modified Reaction Environments for Efficient Catalysis. *ACS Catal.* **7**, 735-765, doi:10.1021/acscatal.6b02603 (2017).

14 Motagamwala, A. H., Almallahi, R., Wortman, J., Igenegbai, V. O. & Linic, S. Stable and selective catalysts for propane dehydrogenation operating at thermodynamic limit. *Science* **373**, 217-222, doi:doi:10.1126/science.abg7894 (2021).

15 Ryoo, R. *et al.* Rare-earth-platinum alloy nanoparticles in mesoporous zeolite for catalysis. *Nature* **585**, 221-224, doi:10.1038/s41586-020-2671-4 (2020).

16 Liu, Y. *et al.* Two-dimensional intermetallic PtBi/Pt core/shell nanoplates overcome tumor hypoxia for enhanced cancer therapy. *Nanoscale* **13**, 14245-14253, doi:10.1039/D1NR02561A (2021).

17 Yang, C.-L. *et al.* Sulfur-anchoring synthesis of platinum intermetallic nanoparticle catalysts for fuel cells. *Science* **374**, 459-464, doi:doi:10.1126/science.abj9980 (2021).

18 Qiu, Y. *et al.* Construction of Pd-Zn dual sites to enhance the performance for ethanol electro-oxidation reaction. *Nat. Commun.* **12**, 5273, doi:10.1038/s41467-021-25600-9 (2021).

19 Maligal-Ganesh, R. V. *et al.* A Ship-in-a-Bottle Strategy To Synthesize Encapsulated Intermetallic Nanoparticle Catalysts: Exemplified for Furfural Hydrogenation. *ACS Catal.* **6**, 1754-1763, doi:10.1021/acscatal.5b02281 (2016).

20 Chong, L. *et al.* Ultralow-loading platinum-cobalt fuel cell catalysts derived from imidazolate frameworks. *Science* **362**, 1276-1281, doi:doi:10.1126/science.aau0630 (2018).

21 Choi, D. S., Robertson, A. W., Warner, J. H., Kim, S. O. & Kim, H. Low-Temperature Chemical Vapor Deposition Synthesis of Pt–Co Alloyed Nanoparticles with Enhanced Oxygen Reduction Reaction Catalysis. *Adv. Mater.* **28**, 7115-7122, doi:https://doi.org/10.1002/adma.201600469 (2016).

22 Cable, R. E. & Schaak, R. E. Reacting the Unreactive: A Toolbox of Low-Temperature Solution-Mediated Reactions for the Facile Interconversion of Nanocrystalline Intermetallic Compounds. *J. Am. Chem. Soc.* **128**, 9588-9589, doi:10.1021/ja0627996 (2006).
23 Clarysse, J., Moser, A., Yarema, O., Wood, V. & Yarema, M. Size- and composition-controlled intermetallic nanocrystals via amalgamation seeded growth. *Sci. Adv.* **7**, eabg1934, doi:doi:10.1126/sciadv.abg1934 (2021).
24 Yao, Y. *et al.* High-entropy nanoparticles: Synthesis-structure-property relationships and data-driven discovery. *Science* **376**, eabn3103, doi:doi:10.1126/science.abn3103 (2022).
25 Chen, A. N. *et al.* Galvanic replacement of intermetallic nanocrystals as a route toward complex heterostructures. *Nanoscale* **13**, 2618-2625, doi:10.1039/d0nr08255d (2021).
26 Yu, J. *et al.* Synthesis of PtSn4 Intermetallic Nanodisks through a Galvanic Replacement Mechanism. *Chem. Mater.*, doi:10.1021/acs.chemmater.2c01381 (2022).
27 Yu, J. *et al.* Precisely Controlled Synthesis of Hybrid Intermetallic–Metal Nanoparticles for Nitrate Electroreduction. *ACS Appl. Mater. Interfaces* **13**, 52073-52081, doi:10.1021/acsami.1c09301 (2021).
28 Sun, Y. & Xia, Y. Shape-Controlled Synthesis of Gold and Silver Nanoparticles. *Science* **298**, 2176-2179, doi:10.1126/science.1077229 (2002).
29 Chee, S. W., Tan, S. F., Baraissov, Z., Bosman, M. & Mirsaidov, U. Direct observation of the nanoscale Kirkendall effect during galvanic replacement reactions. *Nat Commun* **8**, 1224, doi:10.1038/s41467-017-01175-2 (2017).
30 Castilla-Amorós, L., Stoian, D., Pankhurst, J. R., Varandili, S. B. & Buonsanti, R. Exploring the Chemical Reactivity of Gallium Liquid Metal Nanoparticles in Galvanic Replacement. *J. Am. Chem. Soc.* **142**, 19283-19290, doi:10.1021/jacs.0c09458 (2020).
31 Xia, X., Wang, Y., Ruditskiy, A. & Xia, Y. 25th Anniversary Article: Galvanic Replacement: A Simple and Versatile Route to Hollow Nanostructures with Tunable and Well-Controlled Properties. *Adv. Mater.* **25**, 6313-6333, doi:https://doi.org/10.1002/adma.201302820 (2013).
32 Oh, M. H. *et al.* Galvanic Replacement Reactions in Metal Oxide Nanocrystals. *Science* **340**, 964-968, doi:doi:10.1126/science.1234751 (2013).
33 Zhu, Y. *et al.* Inverse iron oxide/metal catalysts from galvanic replacement. *Nat. Commun.* **11**, 3269, doi:10.1038/s41467-020-16830-4 (2020).
34 Wu, Y. *et al.* Dirac node arcs in PtSn4. *Nature Physics* **12**, 667-671, doi:10.1038/nphys3712 (2016).
35 Chen, P.-C. *et al.* Interface and heterostructure design in polyelemental nanoparticles. *Science* **363**, 959-964, doi:doi:10.1126/science.aav4302 (2019).
36 Kravchyk, K. *et al.* Monodisperse and inorganically capped Sn and Sn/SnO2 nanocrystals for high-performance Li-ion battery anodes. *J. Am. Chem. Soc.* **135**, 4199-4202, doi:10.1021/ja312604r (2013).
37 He, M., Protesescu, L., Caputo, R., Krumeich, F. & Kovalenko, M. V. A General Synthesis Strategy for Monodisperse Metallic and Metalloid Nanoparticles (In, Ga, Bi, Sb, Zn, Cu, Sn, and Their Alloys) via in Situ Formed Metal Long-Chain Amides. *Chem. Mater.* **27**, 635-647, doi:10.1021/cm5045144 (2015).

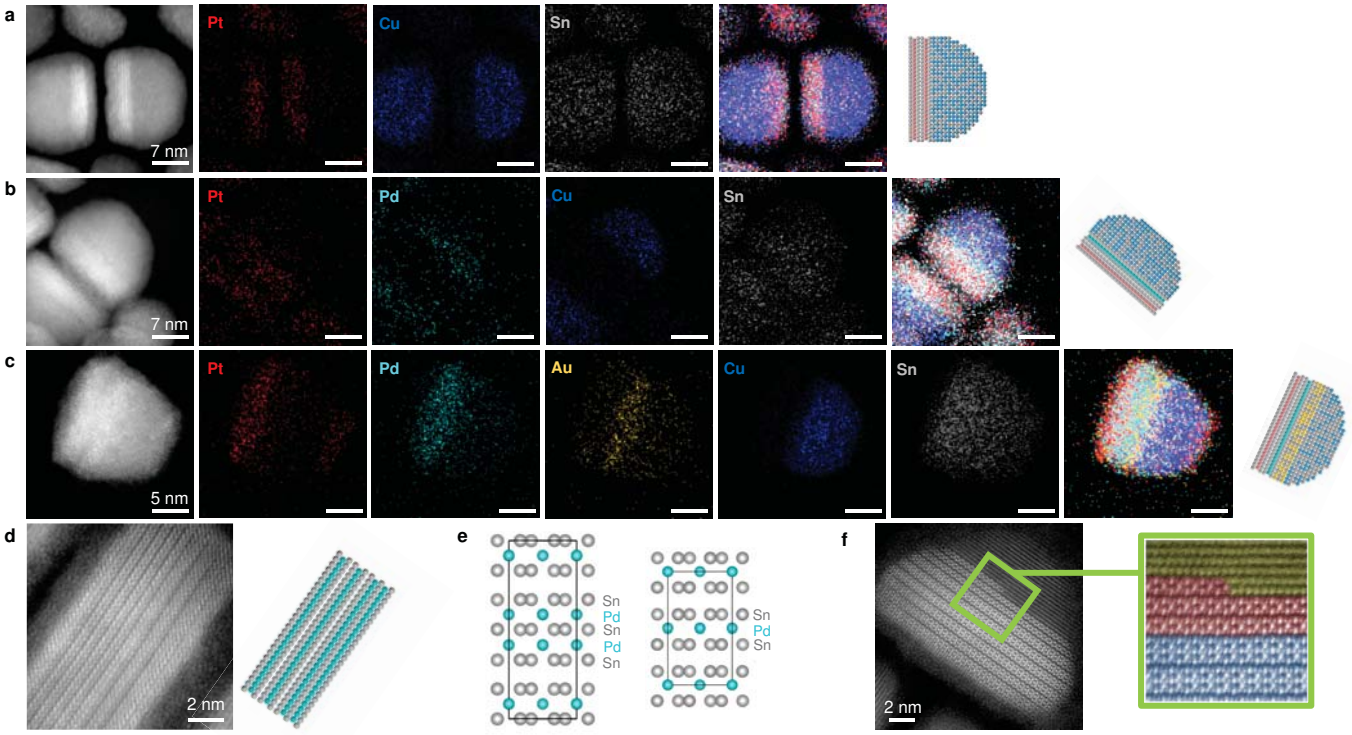
a
Pt
Cu
Sn
7 nm
b
Pt
Pd
Cu
Sn
7 nm
c
Pt
Pd
Au
Cu
Sn
5 nm
d
2 nm
e
Sn
Pd
Sn
Pd
Sn
Sn
Pd
Sn
f
2 nm

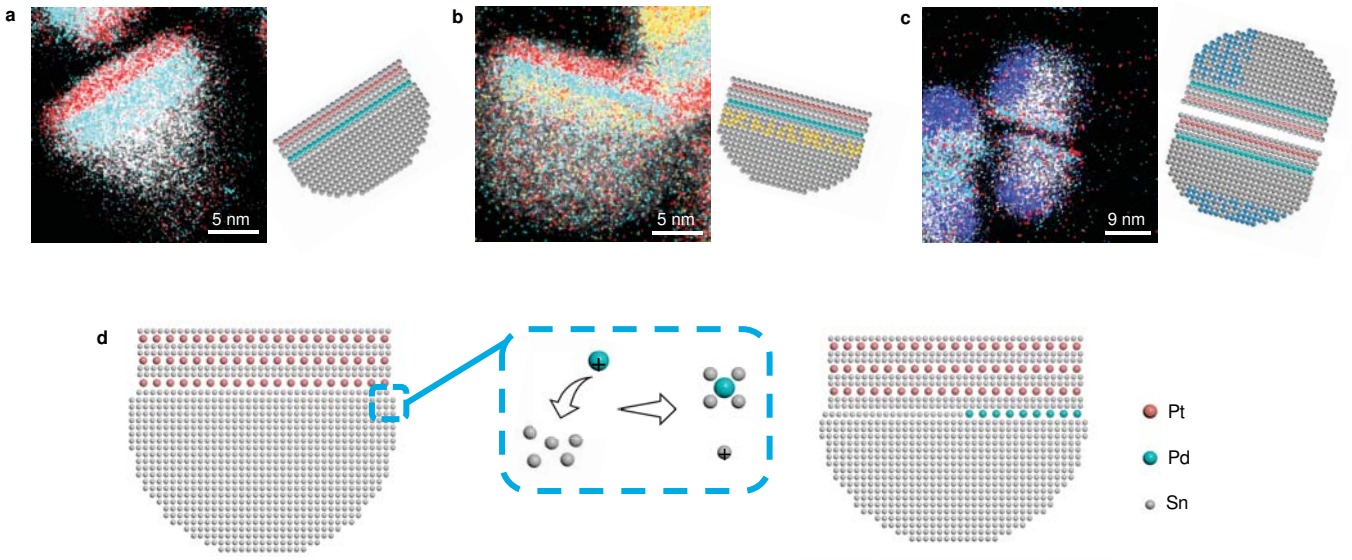
a
5 nm
b
5 nm
c
9 nm
d
Pt
Pd
Sn

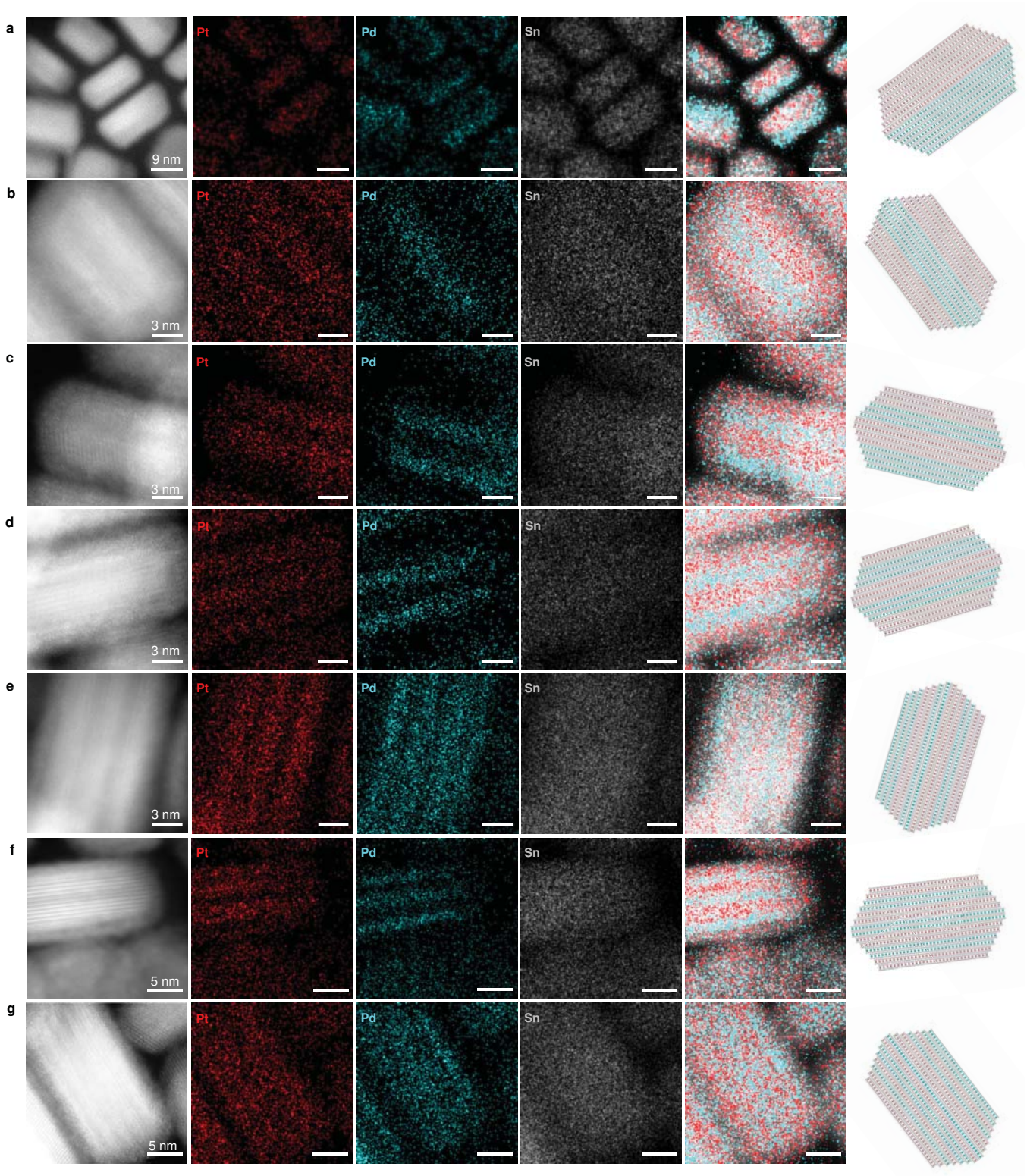
a
Pt
Pd
Sn
9 nm
b
Pt
Pd
Sn
3 nm
c
Pt
Pd
Sn
3 nm
d
Pt
Pd
Sn
3 nm
e
Pt
Pd
Sn
3 nm
f
Pt
Pd
Sn
5 nm
g
Pt
Pd
Sn
5 nm

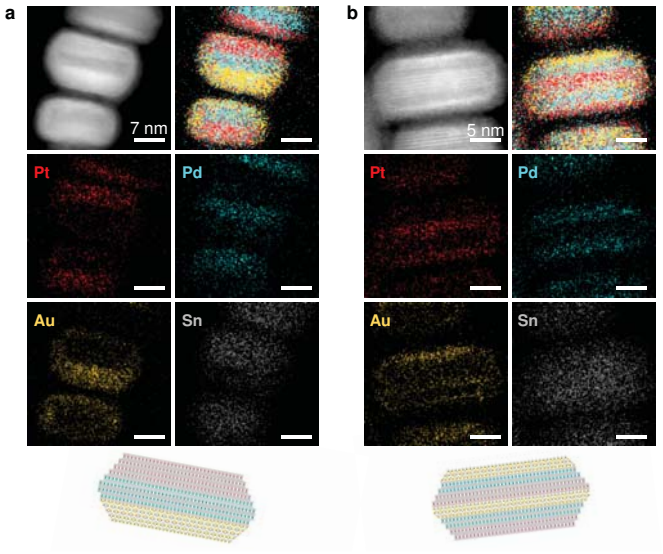
a
7 nm
Pt
Pd
Au
Sn
b
5 nm
Pt
Pd
Au
Sn

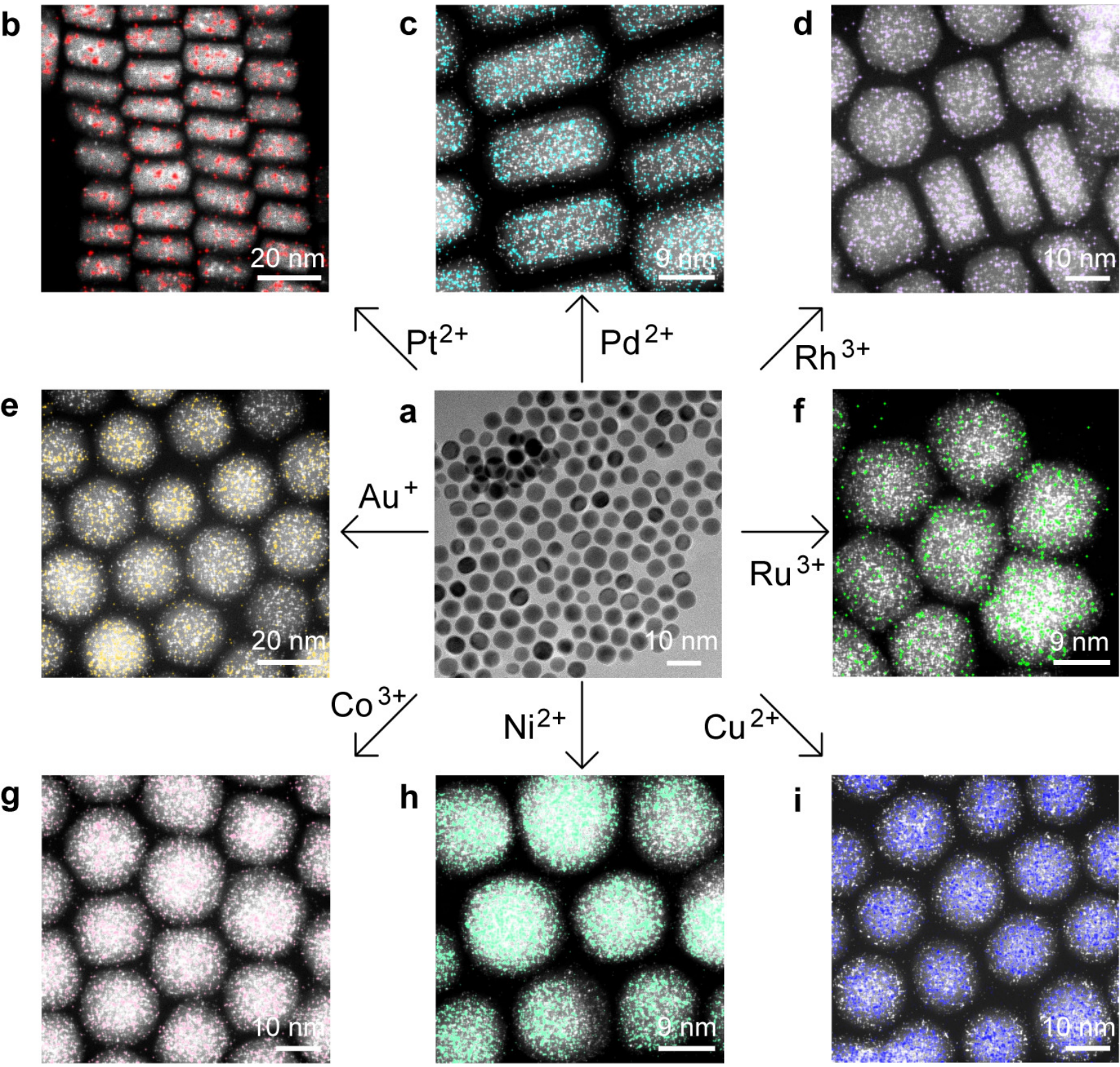
b
20 nm
c
9 nm
d
10 nm
Pt2+
Pd2+
Rh3+
e
20 nm
a
10 nm
f
9 nm
Au+
Ru3+
Co3+
Ni2+
Cu2+
g
10 nm
h
9 nm
i
10 nm

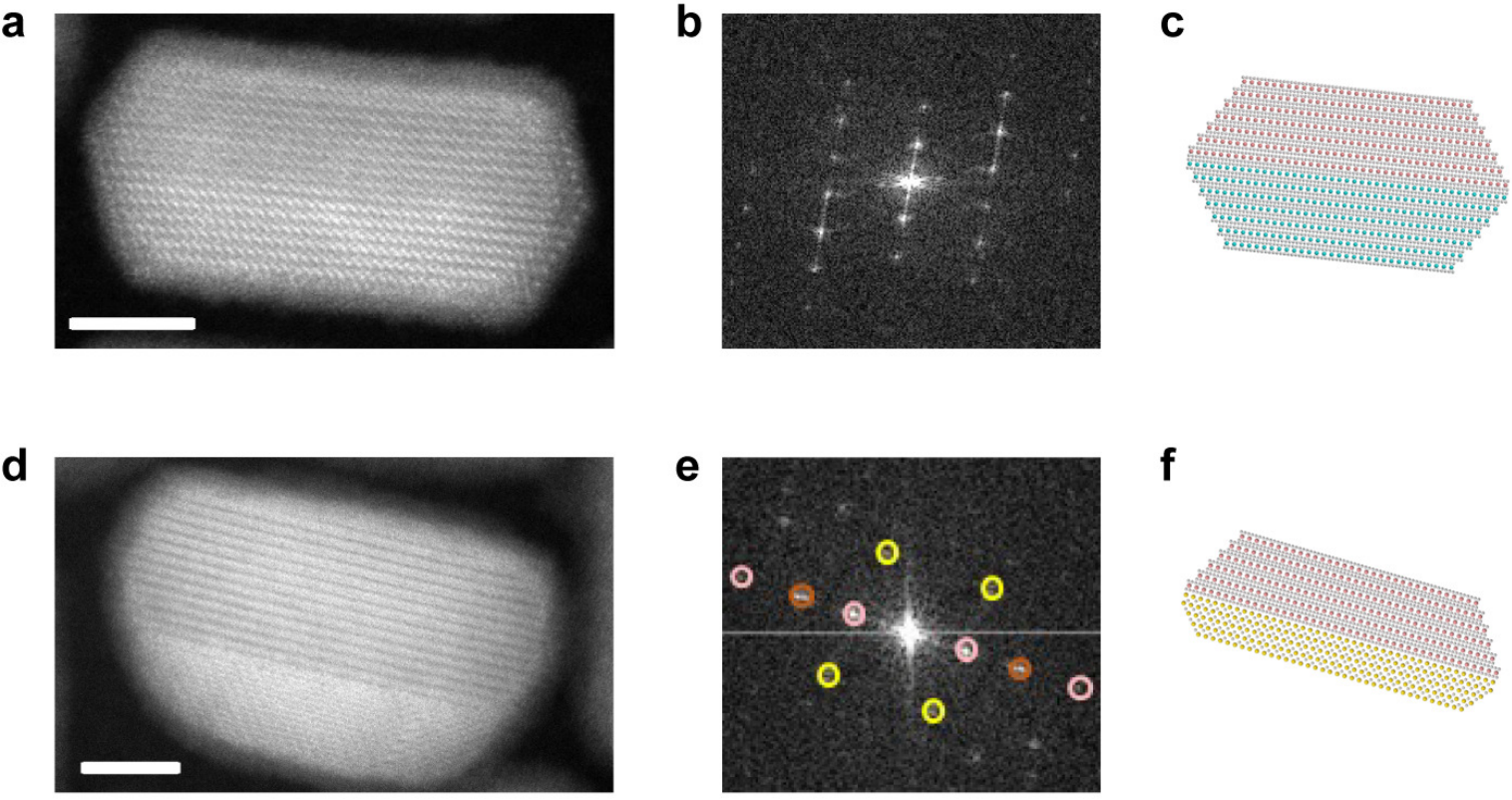
a
b
c
d
e
f